Vibronic Behavior and Single-Crystal EPR Spectra of Cu(II) in Copper-Doped Diaqua(L-aspartato)zinc(II) Hydrate

Marta B. Massa,*,† Sergio D. Dalosto,‡,§ M. Graciela Ferreyra,§ Guillermo Labadie,|| and Rafael Calvo‡,§

Facultad de Ciencias Exactas, Ingeniería y Agrimensura, Universidad Nacional de Rosario, Avda. Pellegrini 250, 2000 Rosario, Argentina, Facultad de Bioquímica y Ciencias Biológicas, Universidad Nacional del Litoral, Casilla 530, 3000 Santa Fe, Argentina, INTEC (CONICET, UNL), Güemes 3450, 3000 Santa Fe, Argentina, and Facultad de Ciencias Bioquímicas y Farmacéuticas, Universidad Nacional de Rosario, Suipacha 570, 2000 Rosario, Argentina

Received: November 17, 1998; In Final Form: January 26, 1999

We investigate the electronic properties of copper ions substituting zinc ions in diaqua(L-aspartato)Zn(II) hydrate ($ZnC_4H_5O_4N\cdot 3H_2O$), to be called Zn(L-asp). In this compound, the Zn ions are in an octahedral coordination with a small distortion in the equatorial plane and the aspartate ion acts as a tridentate ligand. EPR spectra of single crystals of Zn(L-asp) doped with ^{63}Cu(II) were obtained at 9.8 GHz between 77 and 300 K, with the magnetic field applied in the crystallographic planes *ab*, *bc*, and *ca*. The *g*-factor and ^{63}Cu hyperfine coupling along the crystal axes display large temperature variations. From the single-crystal data we obtained the principal values of these tensors: $g_1 = 2.0377(5)$ [2.028(1)], $g_2 = 2.1701(5)$ [2.144(2)], $g_3 = 2.3127(4)$ [2.351(2)], $A_{Cu}^1 = 61.5(4) \times 10^{-4}$ cm^{-1} [$58.0(3) \times 10^{-4}$ cm^{-1}], $A_{Cu}^2 = 20.5(1) \times 10^{-4}$ cm^{-1} [$3.6(3) \times 10^{-4}$ cm^{-1}], $A_{Cu}^3 = 87.8(2) \times 10^{-4}$ cm^{-1} [$114.5(4) \times 10^{-4}$ cm^{-1}], at 300 K [77 K]. At 77 K, the hyperfine coupling with the ^{14}N ligand is resolved and the principal values of the $\mathbf{A}_N$ tensor are $A_N^1 = 11(2) \times 10^{-4}$ cm^{-1}, $A_N^2 = 11(2) \times 10^{-4}$ cm^{-1}, $A_N^3 = 8(2) \times 10^{-4}$ cm^{-1}. EPR data in powder samples at X-band and Q-band were compatible with those values. From the Q-band powder spectrum at 5 K we get $g_1 = 2.03(1)$, $g_2 = 2.12(3)$, $g_3 = 2.36(3)$, $A_{Cu}^1 = 55(1) \times 10^{-4}$ cm^{-1}, $|A_{Cu}^2| = 4(2) \times 10^{-4}$ cm^{-1}, $A_{Cu}^3 = 117(3) \times 10^{-4}$ cm^{-1}, which show the low symmetry of the copper site and are assumed to be the "molecular" parameters. The EPR results are discussed in terms of the structure of Zn(L-asp) and the electronic properties of the copper ions. We analyze the temperature dependence of the *g* and copper hyperfine values considering a dynamic Jahn-Teller effect in terms of a potential surface warped as a consequence of tetragonal and orthorhombic lattice strains. Above 100 K, the behavior is explained in terms of the Boltzmann equilibrium between two isomer configurations distorted along the Cu−water oxygen bond (Silver−Getz model). The energy splitting between the wells are $\delta_{23} = 235(5)$ cm^{-1} and $\delta_{13} \cong 440(50)$ cm^{-1}. Below 100 K, the data indicate the restricted validity of the SG model and suggest that the complex is localized in the deepest well.

1. Introduction

Studies of the structural, electronic, and magnetic properties of metal−amino acid complexes provide valuable information to understand the properties of metal ions in metalloproteins. Metal ions are biologically important and so are their complexes with amino acids.[1] Aspartic and glutamic acids have two carboxylate groups. One belongs to the amino acid group and the other to the terminal group. As a characteristic feature, they may bind metal ions through any of these groups. The structure of the salts of L-aspartic acid with divalent cobalt, zinc, and nickel are isomorphic and crystallize as trihydrates in the orthorhombic space group $P2_12_12_1$.[2−4] That for the copper salt[5] is slightly different, but all the structures reflect that characteristic of the amino acid.

The structure of the zinc salt of aspartic acid was determined by Doyne et al.,[2] who reported only interatomic distances and bond angles. Kryger et al.[3] determined the structure and the positions of all atoms including hydrogens, with results in agreement with those of Doyne et al.[2] Along this work Castellano et al.[6] determined again the structure of Zn(L-asp) using samples grown by us. Their results are of higher accuracy but essentially equal to those of Kryger et al.[3]

The structure of the copper complex of aspartic acid was recently reported.[5] Copper ions have an unpaired spin, and their electronic properties were studied by electron paramagnetic resonance (EPR) spectroscopy. This technique may offer a detailed view of the coordination of the ligands and the chemical bonding of the ion. However, the exchange interactions between copper ions in Cu(L-asp)$(H_2O)_2$ are large enough to collapse to a single line the resonances corresponding to the magnetically nonequivalent copper ions in the lattice and their hyperfine components.[5] This is produced by the so-called "exchange narrowing" phenomenon,[7] which severely limits the information about the electronic properties obtained from the EPR spectra. To recover the information, the magnetic ions have to be introduced as impurities in an isomorphic diamagnetic host lattice. In this case, information may be obtained about the

* Corresponing author. E-mail: mmassa@fceia.unr.edu.ar. Fax: +54-341-4802654.
† Facultad de Ciencias Exactas, Universidad Nacional de Rosario.
‡ Universidad Nacional del Litoral.
§ INTEC.
|| Facultad de Ciencias Bioquímicas y Farmacéuticas.

10.1021/jp984432w CCC: $18.00
Published on Web 03/26/1999

electronic structure and the vibronic interactions as well as features of the hyperfine coupling with the nuclear spins of the metal ion and the ligands.

Here we report an EPR study of ^{63}Cu(II) impurities in single crystals and powdered samples (made by crushing single crystals) of Zn(L-asp) between 300 and 77 K. A powdered sample was also studied at 5 K. Doping with only one isotope improves the EPR resolution and allows us to resolve hyperfine couplings with ligand nuclei at low temperature. We discuss our EPR results in terms of the structure of Zn(L-asp) and the electronic properties of the Cu(II) ions. They are compared to those obtained in Cu(L-asp) in order to learn about the distortions produced at the Zn sites when they are occupied by Cu impurities. We analyze the role of Jahn-Teller distortions in the observed temperature dependence of the *g* and copper hyperfine values. The EPR results and structural data on diluted samples provide information about the nuclear dynamics around the copper impurity. In the zinc lattice, there are not cooperative effects that might obscure the information as in the pure copper complex. Therefore, the experimental data on diluted samples may complete the information about Cu(L-asp), specially in reference to the vibronic behavior.

Theoretical models have been developed in order to analyze the Jahn-Teller effect in a six-coordinated Cu(II) complex with identical ligands and cubic symmetry.[8−15] Silver and Getz (SG)[16] and Riley and Hitchman (RH)[17,18] introduced alternative models to describe the temperature dependence of the *g* and copper hyperfine values for six-coordinated copper complexes in low symmetry sites, under the influence of Jahn-Teller coupling and perturbations due to the surrounding crystal lattices. Variations of the geometry and electronic structure of six-coordinated mixed-ligand Cu(II) complexes with the substitution of a pair of trans ligands by water, ammonia, or other molecules, owing to some symmetry operation, have been studied using a model of dynamic vibronic coupling.[19−22] Here we extend these studies to the case of Cu:Zn(L-asp), where the Cu(II) site has not any point symmetry operation. The observed temperature dependence of the *g* factor and copper hyperfine coupling are discussed for a "pseudo-Jahn-Teller" complex. In this case, the degeneracy of the copper ion is slightly broken by the presence of three different types of ligands which produces a distortion that modifies but does not remove the Jahn-Teller effect.[23]

2. Materials and Methods

2.1. Sample Preparation. Zn(L-asp) was obtained by mixing stoichiometric quantities of a saturated water solution of L-aspartic acid and zinc carbonate hydroxide at 100 °C. The solution was slowly cooled to room temperature. Irregular single crystals with well-resolved (110) faces, obtained at room temperature by slow evaporation of the solution, were separated by filtration. Larger single crystals were grown from solution maintained at 60 °C in a thermostatic bath for several days. Copper-doped single crystals of Zn(L-asp) of up to 3.5 × 2.0 × 1.5 mm were grown for EPR measurements by adding 99% ^{63}Cu-enriched copper(II) nitrate trihydrate and zinc carbonate hydroxide, with about 0.1% Cu/Zn atomic ratio, to the saturated water solution of L-aspartic acid.

2.2. IR and EPR Measurements. Infrared spectra recorded on a Bruker FT I-25 spectrophotometer were analyzed in accordance to the criteria established by Antolini et al.[4,24,25] In the (1650−1350) cm^{-1} wavenumber region characteristic of carboxylate-group vibrations, several bands were observed in agreement with the different coordination of each carboxylate group. Table 1 displays the more relevant IR bands.

TABLE 1: IR Absorptions (cm^{-1}) of Diaqua(L-aspartato)zinc(II) Hydrate (High, 4000; Low, 600; Resolution, 2)

ν (NH_2)	3292
δ (NH_2)	3254
ν $(OCO)_{asym}$	1574, 1556
ν $(OCO)_{sym}$	1422, 1388

The crystal *c* axis of the sample was identified as the intersection of two lateral (110) faces. The sample was glued with GE7031 lacquer in a sample holder made of rexolite according to the crystallographic data, which defines a set *x*(≡*a*), *y*(≡*b*), *z*(≡*c*) of orthogonal axes. This sample holder was positioned in a horizontal plane at the top of a quartz pedestal in the center of the microwave cavity. The EPR measurements were performed at room temperature in a Bruker ER-200 EPR spectrometer working at 9.8 and 35.03 GHz, using a cylindrical cavity with 100 kHz magnetic field modulation. The spectra were obtained with the magnetic field applied in three perpendicular planes *xy*, *yz*, and *zx* at intervals of 5° along a 180° angular range. The positions of the crystal axes within each plane were determined with an accuracy of 1° from the symmetry of the observed angular variation of the *g* factor. EPR measurements at low temperatures were performed at 9.38 GHz, using an immersion Dewar system for temperature control. The temperature was measured with an accuracy of 0.5° using a platinum thermometer. The sample was oriented using the spectra observed at 77 K where the line widths are smaller. Spectra with **B** in the (110) plane were obtained in a sample with this plane glued to the horizontal face of a cubic sample holder. EPR spectra of powdered samples at X and Q-band were also obtained between 5 and 300 K.

3. Crystal Structure Data

3.1. Crystal and Molecular Structure of Zn(L-asp). The crystal structure of diaqua(L-aspartato)Zn(II) hydrate ($ZnC_4H_5O_4N\cdot 3H_2O$) was determined at room temperature.[2,3] It was redetermined by Castellano et al.[6] along this work, and we use these newer and more accurate results in our analysis. Zn(L-asp) crystallizes in the orthorhombic space group $P2_12_12_1$, with a = 9.338(1) Å, b = 7.8066(7) Å, c = 11.550(1) Å, and z = 4.

In Zn(L-asp), each aspartate ion acts as a tridentate ligand through the nitrogen (N), one oxygen (O1) from the α-carboxylate group, and one oxygen (O4) from the *β*-carboxylate group. Each Zn ion has a nitrogen (N) and three oxygens (O1 from the α-carboxylate group and O3′ from a *β*-carboxylate group of a neighbor aspartate molecule and Ow2 belonging to a water molecule) as equatorial ligands. Two oxygens (O4 from the *β*-carboxylate group and Ow1 belonging to another water molecule) complete the octahedron of ligands at apical positions. The Zn coordination in Zn(L-asp) (Figure 1a) is octahedral with a small tetragonal deformation but a well-defined equatorial plane. (The dashed axis in Figure 1a indicates the direction of the normal to the equatorial plane). There are four symmetry-related molecules in the unit cell (z = 4). Figure 1b showing the molecules I, II, III, and IV will be used in the analysis of the EPR results. Molecules II, III, and IV are obtained from molecule I by 180° rotations around the axes *c*, *a*, and *b*, plus a translation, respectively. The bond distances are given in Figure 2. The angles between Zn and the coordinated ligands are given in Table 2.

At each direction of the octahedron there is a ligand with two protons (Ow1, Ow2, N) and opposite to it there is an oxygen (O1, O4, O3′) from a carboxylate group (angles: ZnO4C4 = 127.9(1)°, ZnO1C1 = 109.9(1)°, ZnO3'C4 = 122.3(1)°) (see

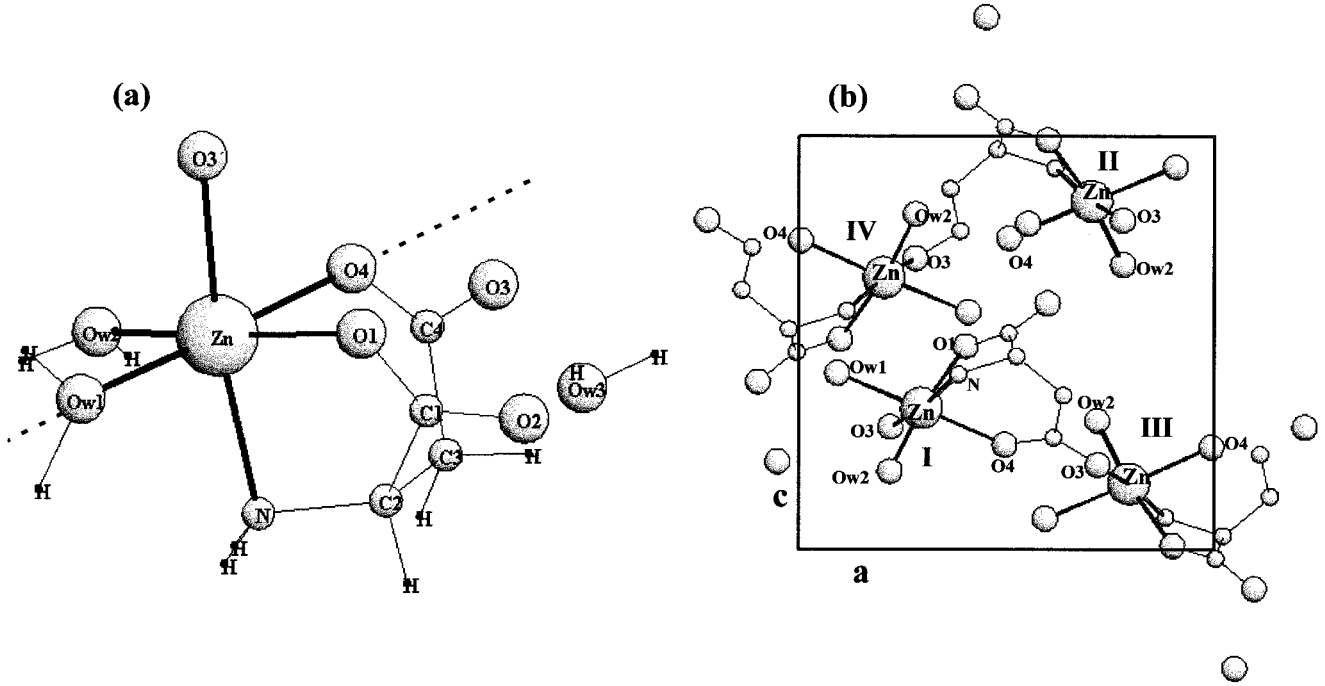

Figure 1. (a) Molecular structure of Zn(L-asp), showing the labeling of the atoms, the environment of the zinc atom, and the aspartate molecule. The meaning of the dashed axis is discussed in the text. (b) Orientation of the four symmetry related zinc molecules in the unit cell projected onto the *ac* plane. Site I is that given in the crystal structure determination.[6]

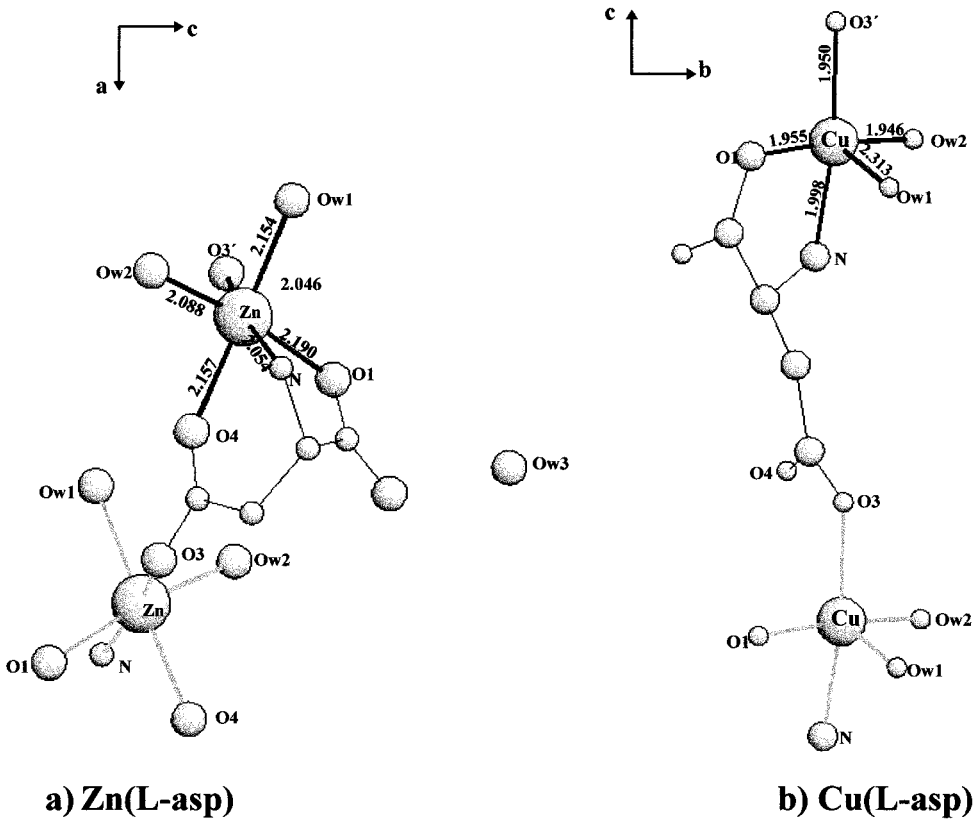

Figure 2. Projections of the structures of Zn(L-asp) (a) and Cu(L-asp) (b) onto the *ac* and *bc* planes, respectively. Bond distances are in angstroms. From data of refs 5 and 6.

Figure 1a). The asymmetry introduced by the difference between a N and a water O ligand produces a distortion of the Zn molecule (see Figure 1a). Furthermore, the nitrogen ligand is displaced toward the oxygen ligand (O1) as a consequence of the rigid bonds in the α-carboxylate group. This introduces an additional angular distortion in the equatorial plane (angle: O1ZnN = 77.8(1)°) lowering the Zn(II) local symmetry which, however, is close to C_2.

The internal molecular motion is reflected by the thermal displacement tensor **U** obtained from the crystal data.[6] Zn and N atoms are described by nearly isotropic thermal displacements, while anisotropic ones describe the oxygen atoms. The atomic

TABLE 2: Comparison of the Structural Features of the Zn and Cu Complexes with Aspartic Acid

	Zn(L-asp) (from ref 6)	Cu(L-asp) (from ref 5)
space group	$P2_12_12_1$	C_2
coordination of metal ion	distorted octahedral	tetragonally distorted square pyramidal
bond angles in the plane		
O1−metal−Ow2	172.80(8)	172.6(1)°
O1−metal−N	77.84(8)	83.4(1)°
O1−metal−O3′	89.08(8)	90.9(1)°
O1−metal−Ow1	96.01(8)	91.8(1)°
N−metal−O3′	166.73(9)	168.4(1)°
N−metal−Ow2	101.39(9)	89.4(1)°
O3′−metal−Ow2	91.87(8)	95.9(1)°
N−metal−Ow1	91.68(9)	96.8(1)°
Ow1−metal−Ow2	91.16(8)	90.6(1)°
Ow1−metal−O3′	87.43(8)	93.5(1)°
O4−metal−O1	85.25(8)	
O4−metal−Ow2	87.59(8)	
O4−metal−N	89.64(9)	
O4−metal−O3′	91.51(8)	
O4−metal−Ow1	178.34(8)	
water molecules coordination	2	2
water hydration molecules	1	
aspartate ion ligand	tridentate	bidentate
distance of the metal to the least-squares equatorial or base plane (in Å)	0.952(1) toward Ow1	0.107(1) toward Ow1
apical ligand distances to least-squares equatorial or base plane (in Å)	3.102(2) (Ow1) 1.204(2) (O4)	2.17(2) (Ow1) 1.96(2) (O4)

mean-square displacements $\langle \Delta U^2 \rangle = \mathbf{I}\cdot\mathbf{U}(\mathrm{Zn})\cdot\mathbf{I} - \mathbf{I}\cdot\mathbf{U}(\mathrm{ligand})\cdot\mathbf{I}$[18] along the directions **I** defined by the Zn ion and each ligand are: $(\Delta U^2_{\mathrm{Zn-Ow1}}) = 0.004(1)$ Å^2, $(\Delta U^2_{\mathrm{Zn-Ow2}}) = 0.006(1)$ Å^2, $(\Delta U^2_{\mathrm{Zn-O4}}) = 0.001(1)$ Å^2, $(\Delta U^2_{\mathrm{Zn-O1}}) = 0.003(1)$ Å^2, $(\Delta U^2_{\mathrm{Zn-O3'}}) = 0.001(1)$ Å^2, and $(\Delta U^2_{\mathrm{Zn-N}}) = 0.003(1)$ Å^2.

3.2. Comparison with Cu(L-asp). The Cu(II) ion in Cu(L-asp) is in a distorted tetragonal pyramidal coordination.[5] It is in the plane of the base of the pyramid with an environment similar to that described for the metal in the equatorial plane ion in Zn(L-asp) (see Figure 2a,b). Bond distances are shorter than those for Zn(L-asp), because the ionic radius of Cu(II) ($r = 0.69$ Å) is shorter than that of Zn(II) ($r = 0.76$ Å). The 5-fold coordination is completed with a far oxygen of a second water molecule (Ow1) at the top of the pyramid. At each direction defined by the ligands in the base of the pyramid there is a ligand with two protons (Ow2, N), and opposite to it an oxygen of a carboxylate group (angle CuO1C1 = 115.6(1)°, angle CuO3C4 = 115.0(1)°). The copper ion is displaced 0.107(1) Å from the least-squares plane defined by N, O1, Ow2, and O3′, toward the apical water oxygen Ow1. Meanwhile, Zn(II) in Zn(L-asp) is in the equatorial plane within experimental error. The Cα−COO atoms in the aspartate molecule in Cu(L-asp) are coplanar within experimental errors. This tendency is lost in Zn(L-asp) where the C2 atom is forced to stand out of this plane when the Cβ−COO atoms coordinate to the Zn ion through its apical ligand O4. In both complexes, Cβ−COO atoms are coplanar. The dihedral angle between the α and β carboxylate least-squares planes changes from 85.9(1)° (Cu(L-asp)) to 14.0(1)° (Zn(L-asp)), as a consequence of the O4−Zn bond. The angles between the Cα−COO and Cβ−COO planes and the least-squares plane of ligands around the metal site are 10.0(6)° [92.7(6)°] and 85.9(1)° [98.57(6)°] in Cu(L-asp) [Zn(L-asp)], respectively. The atomic mean-square displacements $\langle \Delta U^2 \rangle$ along the direction **I** defined by the Cu and each ligand obtained from the data in ref 5 are $(\Delta U^2_{\mathrm{Cu-Ow1}}) = 0.002(1)$ Å^2, $(\Delta U^2_{\mathrm{Cu-Ow2}}) = 0.004(1)$ Å^2, $(\Delta U^2_{\mathrm{Cu-O1}}) = 0.004(1)$ Å^2, $(\Delta U^2_{\mathrm{Cu-O3'}}) = 0.002(1)$ Å^2, and $(\Delta U^2_{\mathrm{Cu-N}}) = 0.002(1)$ Å^2. These mean-square thermal displacements, like those given above for Zn(L-asp), have the small magnitude expected for intramolecular stretching motion[26] along the metal−ligand bond.

The main structural features of Zn(L-asp) and Cu(L-asp) (refs 6 and 5) are summarized in Table 2. In both compounds, the aspartate ion links two metal sites, generating covalently bonded −metal−asp−metal−asp−metal− chains along the *c* axis (Cu(L-asp)) and the *a* axis (Zn(L-asp)). It acts in one side as bidentate in (Cu(L-asp)) or tridentate in Zn(L-asp) ligand and through an oxygen of a β-carboxylate group in the other side (see Figure 2a,b).

4. EPR Results

4.1. Single-Crystal EPR Studies. Two groups of four EPR lines are observed in single crystals of Cu:Zn(L-asp) for arbitrary orientations of the magnetic field **B** within the planes *ab*, *bc*, and *ac* (see Figure 3b,d) at 300 K. They collapse into a single group of four EPR lines for **B** along each crystal axis (see Figure 4a). The spectrum becomes too complicate when **B** is applied in a general direction out of the crystallographic planes. It is compatible, however, with the existence of four groups, each having four hyperfine components. The EPR lines narrow when the temperature decreases (see Figure 3), and at 77 K each ^{63}Cu hyperfine component displays an additional three-line nitrogen superhyperfine pattern due to interactions with one nitrogen nuclei ($I(^{14}\mathrm{N}) = 1$) (see Figures 3a,c and 4a). EPR spectra with **B** along the crystal axes were also obtained as a function of temperature between 300 and 77 K (see Figure 4a).

4.2. EPR Spectra of Powdered Samples. EPR spectra of powdered samples were measured between 77 and 300 K at 9.38 GHz and between 5 and 300 K at 35.03 GHz. Some spectra are shown in Figure 4b. They are typical for copper in a tetragonally elongated octahedral geometry with an orthorhombic distortion.

5. Analysis of the EPR Data

5.1. Spin Hamiltonian. The spin Hamiltonian describing the energy levels relevant to the EPR experiments is[27]

$$H = \sum_{\alpha=\mathrm{I-IV}} [\mu_B \mathbf{S}_\alpha\cdot\mathbf{g}_\alpha\cdot\mathbf{B} + \mathbf{I}_\alpha\cdot\mathbf{A}_{\mathrm{Cu}\alpha}\cdot\mathbf{S}_\alpha + \mathbf{I}_\alpha\cdot\mathbf{A}_{\mathrm{N}\alpha}\cdot\mathbf{S}_\alpha] \quad (1)$$

where μ_B is the Bohr magneton, $\mathbf{g}_\alpha$, $\mathbf{A}_{\mathrm{Cu}\alpha}$, and $\mathbf{A}_{\mathrm{N}\alpha}$ are the *g*, copper hyperfine, and nitrogen hyperfine tensors, respectively, for copper ions in the site α (α = I−IV) of the structure of Zn(L-asp). The first term of eq 1 is the Zeeman interaction of the effective spin $S = 1/2$ of copper ions with the external magnetic field **B**, which gives rise to one resonance for each copper site. The second term is the hyperfine interaction between **S** and the nuclear spin $I = 3/2$ of ^{63}Cu which splits these resonances into four components. The third term is the hyperfine interaction with the nuclear spin $I(^{14}\mathrm{N}) = 1$ of the nitrogen ligand in the equatorial plane. It produces an additional splitting of each resonance into three components. The tensors $\mathbf{g}_\alpha$, $\mathbf{A}_{\mathrm{Cu}\alpha}$, and $\mathbf{A}_{\mathrm{N}\alpha}$ for the different α are related by C_2 rotations around the crystal axes. The energy levels of this spin Hamiltonian have been calculated up to second order in a perturbative approach by Weil,[27] and we use his results to analyze our experimental data. For each α site, the position in the magnetic field of the EPR transition ($M = 1/2$, m_{Cu}, m_{N}) ↔ ($M = -1/2$, m_{Cu}, m_{N}) for $S = 1/2$ is

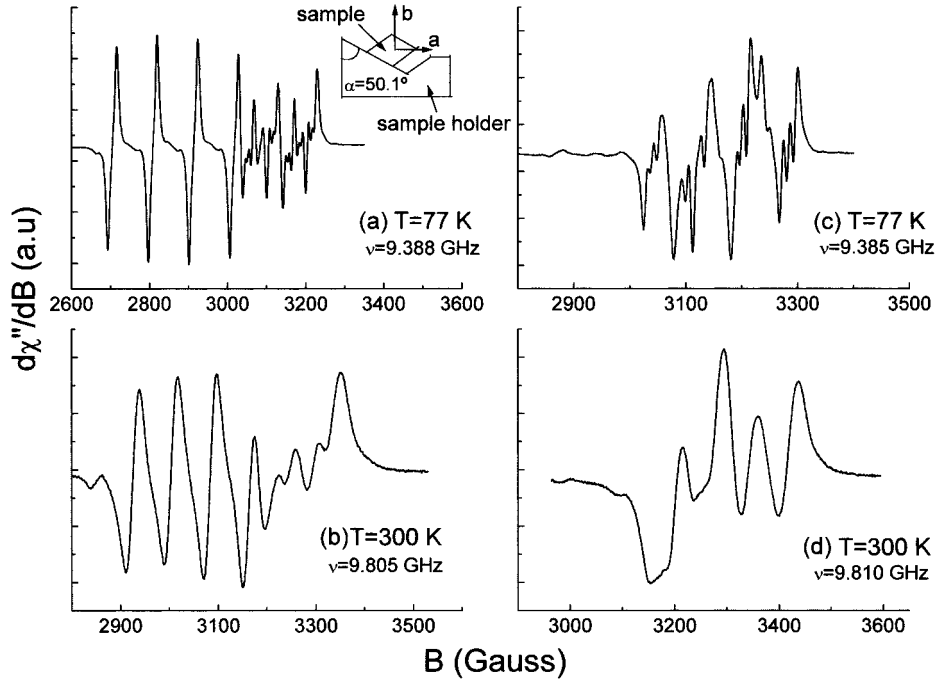

Figure 3. Single-crystal EPR spectra of ^{63}Cu in Zn(L-asp) obtained for different magnetic field orientations and temperatures: (a) $\vartheta = 30°$, $\varphi = 90°$, $T = 77$ K; (b) $\vartheta = 30°$, $\varphi = 90°$, $T = 300$ K; (c) $\vartheta = 50°$, $\varphi = 50°$, $T = 77$ K; (d) $\vartheta = 50°$, $\varphi = 50°$, $T = 300$ K. The polar and azimuthal angles ϑ and φ are defined in the $x(\equiv a)$, $y(\equiv b)$, $z(\equiv c)$ system of axes. In (b), the spectrum shows two groups of four ^{63}Cu hyperfine lines, corresponding to the two magnetically nonequivalent sites for Cu(II). At 77 K, the spectra have an additional superhyperfine structure due to the nitrogen ligand $I(^{14}\mathrm{N}) = 1$.

$$B(m_{Cu},m_N) = \{h\nu_o/g\mu_B - K_{Cu}m_{Cu}/g\mu_B - K_N m_N/g\mu_B - [(\mathrm{Tr}(\mathbf{A}_{Cu}\cdot\mathbf{A}_{Cu}) - k_{Cu}^2)I_{Cu}(I_{Cu}+1)]/(4g_\alpha^2\mu_B^2 B)\} + \sum(m_{Cu}^2/2g^2\mu_B^2 B)\{1/2\mathrm{Tr}(\mathbf{A}_{Cu}\cdot\mathbf{A}_{Cu}) + K_{Cu}^2 - 3/2k_{Cu}^2\} \quad (2)$$

where ν_o is the microwave frequency, $\eta = \mathbf{B}/|\mathbf{B}|$ is the direction of the applied magnetic field, and $g = (\eta\cdot\mathbf{g}\cdot\mathbf{g}\cdot\eta)^{1/2}$, $gK_i = (\eta\cdot\mathbf{g}\cdot\mathbf{A}_i\cdot\mathbf{A}_i\cdot\mathbf{g}\cdot\eta)^{1/2}$ and $gK_ik_i = (\eta\cdot\mathbf{g}\cdot\mathbf{A}_i\cdot\mathbf{A}_i\cdot\mathbf{A}_i\cdot\mathbf{A}_i\cdot\mathbf{g}\cdot\eta)^{1/2}$ are the projections of the tensors $\mathbf{g}$, $\mathbf{g}\cdot\mathbf{A}_i$ and $\mathbf{g}\cdot\mathbf{A}_i\cdot\mathbf{A}_i$ along the direction η (i = Cu, N) for each site α (see eq 1).

5.2. Tensors g, $\mathbf{A_{Cu}}$, and $\mathbf{A_N}$ from Single-Crystal Data. The components of the tensors $\mathbf{g}_\alpha$, $\mathbf{A}_{Cu\alpha}$, and $\mathbf{A}_{N\alpha}$ defined in eq 1 were obtained from the data using eq 2 following the procedure described by Calvo et al.[28] Second-order contributions to the positions of the resonance fields and to the hyperfine coupling were considered in a numerical iterative process until agreement was obtained between the predictions of eq 2 and the data. At room temperature, superhyperfine interactions with nitrogen nuclei were not resolved, and therefore they were omitted in the analysis. The positions $B_\alpha(m_{Cu})$ of the resonances for each orientation of **B** were obtained by simulating the observed (digitalized) spectra with the sum of two sets of four resonances, using a nonlinear least-squares program. Gaussian line shapes were found to be in good agreement with the data. These simulations allowed calculating the positions and line widths of each hyperfine component. Each set of four resonances was assigned to a pair of magnetically equivalent sites according to the symmetry relations, that is, pairs I−II and III−IV in the *ab* plane, I−III and II−IV in the *bc* plane, and I−IV and II−III in the *ca* plane (see Figure 1b). When **B** is along any of the three crystallographic axes, the observed spectra (Figure 4a) were simulated with only one set of four resonances. The positions $B(m_{Cu},m_N)$ of the resonances in the spectra having resolved superhyperfine interactions were simulated by the sum of a set of four groups (associated with each value of m_{Cu}) of three resonances (for $m_N = -1,0,1$) for each nonequivalent copper ion (one set for **B** along the axes and two sets in the crystalline planes).

The values of $g^2(\vartheta,\varphi)$ and $g^2K_{Cu}^2(\vartheta,\varphi)$ calculated from the data in the three planes at 300 and 77 K and of $g^2K_N^2(\vartheta,\varphi)$ measured in the three planes, at 77 K, are shown in Figure 5. The superhyperfine coupling could be resolved only for few orientations of **B** within the *bc* plane. The experimental results were used to calculate the components of the symmetric tensors $\mathbf{g}\cdot\mathbf{g}$, $\mathbf{g}\cdot\mathbf{A}_{Cu}\cdot\mathbf{A}_{Cu}\cdot\mathbf{g}$ and $\mathbf{g}\cdot\mathbf{A}_N\cdot\mathbf{A}_N\cdot\mathbf{g}$ using a least-squares program.

The results in the different planes were combined in order to obtain the spin-Hamiltonian parameters for each Cu(II) site (α = I−IV in eq 1). However, we obtain for the tensors $\mathbf{g}\cdot\mathbf{g}$, $\mathbf{g}\cdot\mathbf{A}_{Cu}\cdot\mathbf{A}_{Cu}\cdot\mathbf{g}$ and $\mathbf{g}\cdot\mathbf{A}_N\cdot\mathbf{A}_N\cdot\mathbf{g}$ eight possible sets of components, instead of the four corresponding to the sites I, II, III, and IV, shown in Figure 1b. They differ only in the signs of the nondiagonal components. After diagonalization, these eight tensors may be divided into two groups (A and B) of four tensors, each group having the same eigenvalues. The pairwise magnetic equivalence of the sites in the crystalline planes inhibited the determination of the relative signs of the nondiagonal elements of the tensors and thus to single out one group of parameters for Cu:Zn(L-asp). To choose the physically real group of four $\mathbf{g}\cdot\mathbf{g}$ and $\mathbf{g}\cdot\mathbf{A}_{Cu}\cdot\mathbf{A}_{Cu}\cdot\mathbf{g}$ tensors, one should have data taken for the magnetic field outside of the crystallographic planes. However, this is difficult because of the complexity and low resolution of the spectra for these orientations. To solve the problem, we used three different methods. In the first one, we simulated the powder spectrum of Cu:Zn(L-asp) (Figure 4b) with the two sets (A and B) of $\mathbf{g}$ and $\mathbf{A}_{Cu}$ tensors obtained from the single-crystal EPR results. The nitrogen superhyperfine coupling was considered in the analysis at 77 K. We found that tensors of the group A simulate well the powder spectra observed at each temperature while those of group B give a poor simulation. In the second method, we analyzed the angular variation of the spectra with **B** in the (110) plane, as proposed

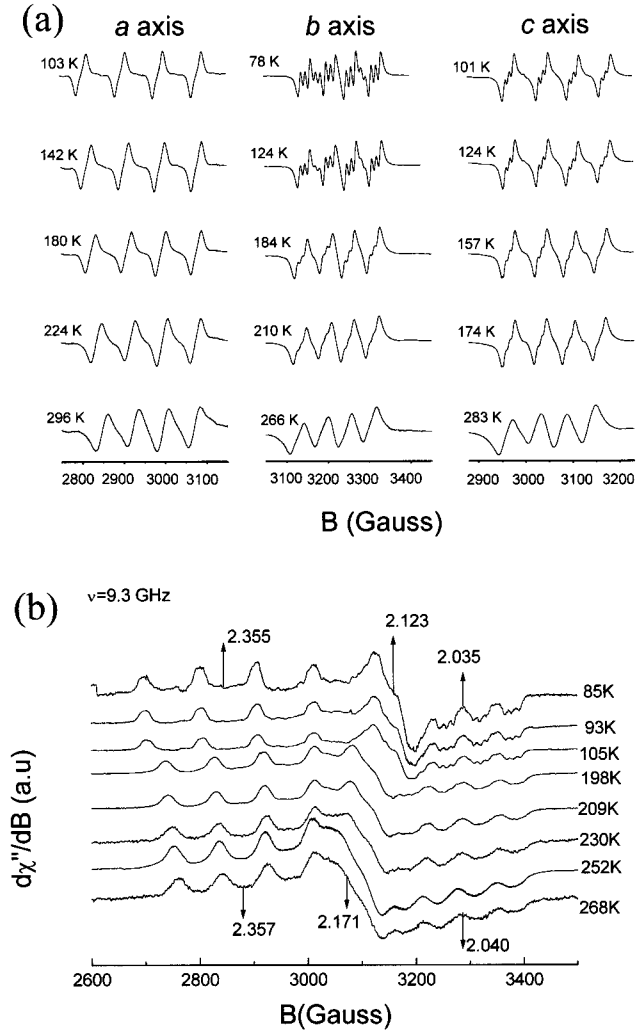

Figure 4. (a) EPR spectra of ^{63}Cu impurities in a Zn(L-asp) single crystal, shown as a function of temperature in the range (77, 300) K, with the magnetic field **B** oriented along the *a*, *b*, and *c* axes. For these field orientations, the spectra of the four copper sites collapse to one, showing that all four sites are equivalent. (b) EPR spectra of powdered Cu(II) doped in Zn(L-asp) measured at different temperatures at 9.38 GHz.

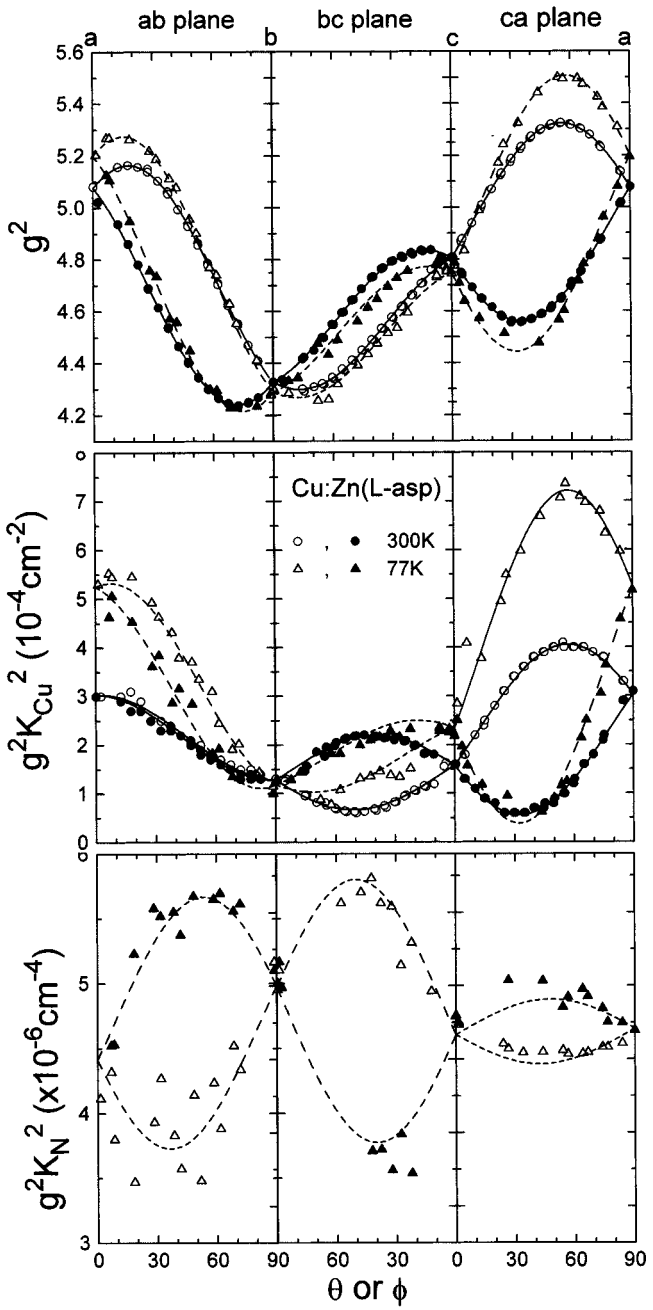

Figure 5. Observed angular variation of $g^2(\vartheta,\varphi)$, $g^2K_{Cu}^2(\vartheta,\varphi)$ and $g^2K_N^2(\vartheta,\varphi)$ for a ^{63}Cu-doped Zn(L-asp) crystal at 300 and 77 K for the magnetic field applied in the *ab*, *bc*, and *ca* crystalline planes. The solid lines are calculated with the components of the tensors $\mathbf{g}\cdot\mathbf{g}$ and $\mathbf{g}\cdot\mathbf{A}_{Cu}\cdot\mathbf{A}_{Cu}\cdot\mathbf{g}$ given in Table 3.

by Isaacson et al.[29] However, instead of the positions of the resonances, we compared the span in field of the spectra observed in the (110) plane with that of the simulated spectra calculated with each group of tensors. Figure 6 shows the experimental results for this span, together with the values calculated with the groups A and B of parameters. Again, group A provides the best agreement with the experimental data. In the third method, the principal directions of the tensors **g** and $\mathbf{A}_{Cu}$ for the groups A and B were compared to the structural data. We observe that the principal directions of these tensors for the group A are associated with the Cu−N, Cu−Ow2, and Cu−Ow1 directions for each of the four sites I, II, III, and IV, as is shown for one of these in Figure 7. However, no relation with the metal−ligand bonds are found for the principal directions of the tensors **g** and $\mathbf{A}_{Cu}$ of the group B. The agreement between the results obtained with the three methods indicates that the valid solution for the tensors corresponds to the group A. The eigenvalues and eigenvectors of the tensors **g** and $\mathbf{A}_{Cu}$ were calculated from the $\mathbf{g}\cdot\mathbf{g}$ and $\mathbf{g}\cdot\mathbf{A}_{Cu}\cdot\mathbf{A}_{Cu}\cdot\mathbf{g}$ tensors belonging to this group. Eigenvalues and eigenvectors of $\mathbf{A}_N$, calculated from the data at 77 K, have large uncertainties due to the difficulties in simulating the spectra on the *bc* plane where the positions in field of the lines for the two nonequivalent sites are too close. The results at room temperature and at 77 K are given in Table 3.

5.3. Analysis of the Spectra of Powder Samples. The powder spectra were simulated using the program QPOW.[30−32] The Q-band spectra show a temperature dependence of the eigenvalues of **g** and $\mathbf{A}_{Cu}$ between 5 and 300 K. The EPR data at 5 K are summarized in Table 3 for completeness.

5.4. Temperature Variation of the *g*-Factor and Hyperfine Coupling from Single-Crystal Spectra. The significant differences observed between the *g*-factors and hyperfine coupling measured at 300 and 77 K (see Figures 3 and 4) lead us to study the temperature dependence of the *g*-factor and hyperfine coupling on a single crystal at 9.8 GHz. It is very difficult to

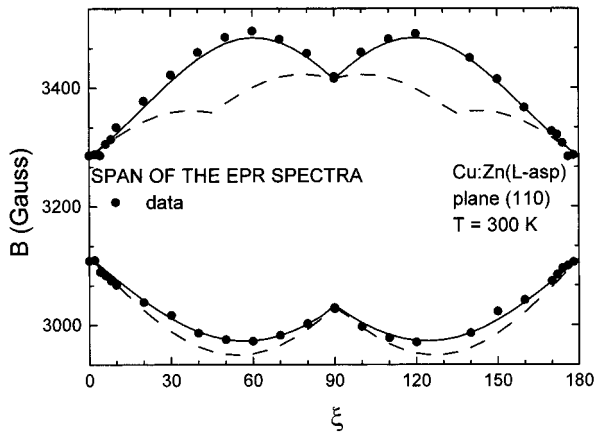

Figure 6. Span of the resonance fields of Cu:Zn(L-asp) for the magnetic field **B** within the (110) plane. The angle $\xi = 0$ corresponds to the *c* axis. The solid circles are the observed maximum and minimum field position of the EPR spectra. The solid line, calculated with the tensors **g** and $\mathbf{A}_{Cu}$ in the A group (Table 3), is in good agreement with the data. The dashed line is calculated with the tensors in the B group.

keep the temperature stable for times long enough to measure the full angular variation of the spectra at intermediate temperatures between 77 and 300 K. Therefore, the spectra were measured as a function of temperature only for **B** along each crystalline axis. Thus, only the diagonal components of the $\mathbf{g}^2(T)$ and $\mathbf{A}_{Cu}$ tensors in the (*a*,*b*,*c*) axes system can be determined from these spectra (see Figure 4a). The principal molecular *g*-values as a function of *T* were obtained by diagonalization of the $\mathbf{g}^2(T)$ tensor:

$$L\cdot\mathbf{g}^2(T)\cdot L = \mathbf{g}_d{}^2(T) \tag{3}$$

where $\mathbf{g}^2(T)$ is a symmetric tensor obtained from the experiment at different temperatures, and $\mathbf{g}_d{}^2(T)$ is the diagonal tensor at the temperature *T*. $L = [l_{ij}]$ is the transformation matrix from the (*a*,*b*,*c*) axes to the principal axes. The same procedure was used to calculate the eigenvalues of $\mathbf{g}\cdot\mathbf{A}_{Cu}\cdot\mathbf{A}_{Cu}\cdot\mathbf{g}$ as a function of *T* from the spectra measured along the crystal axes. Table 3 shows that the eigenvectors of **g** and $\mathbf{A}_{Cu}$ do not change when going from 300 to 77 K. Thus, we assume that the l_{ij} are temperature independent, and we use their values to obtain the principal values ($g_1{}^2$, $g_2{}^2$, $g_3{}^2$) of $\mathbf{g}_d{}^2(T)$, using eq 3. These results are plotted in Figure 8a.

5.5. Summary of the Experimental Results. The experimental results to be explained are as follows.

(i) At 300 K, the tensors **g** and $\mathbf{A}_{Cu}$ have orthorhombic symmetry (see Table 3), with their eigenvectors coincident within experimental uncertainties. One principal value (g_2 and $A_{Cu}{}^1$), lying midway between the other two, is along the Zn−Ow2 direction. The largest eigenvalues (g_3 and $A_{Cu}{}^3$) are along the normal to the equatorial plane, parallel to the Zn−Ow1 bond. The smallest eigenvalues (g_1 and $A_{Cu}{}^2$) are on the equatorial plane, along the Zn−N and Zn−Ow2 directions, respectively. The eigenvectors of the tensors **g** and $\mathbf{A}_{Cu}$ do not change with temperature from 300 to 77 K and may be considered as the molecular axes.

(ii) The $\mathbf{A}_N$ tensor calculated from the data has axial symmetry around the Cu−N bond (see Table 3).

(iii) The temperature variations of g^2 and $g^2K_{Cu}{}^2$ are largest for **B** along the *a* axis, smaller but significative along the *c* axis, and negligible along the *b* axis (see Figure 5).

(iv) The principal values g_2 and g_3; $A_{Cu}{}^2$ and $A_{Cu}{}^3$ display a linear dependence with the temperature *T*, but g_1 does not change with *T* and $A_{Cu}{}^1$ is very weakly dependent. $A_{Cu}{}^2$ is small at room temperature. As it decreases when cooling, the analysis of Figure 8b indicates that it should be negative at low temperature. This tendency is similar to that found in Cu:Zn Tutton's salt[33] where the authors left the sign of $A_{Cu}{}^2$ undetermined.

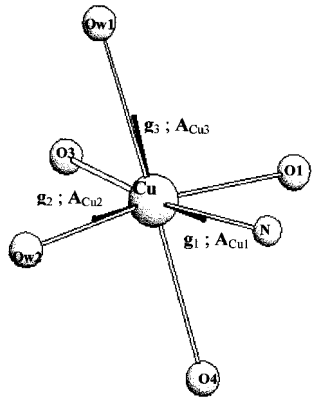

Figure 7. Principal directions of the **g** tensor for Cu:Zn(L-asp). The principal directions of the ^{63}Cu(II) hyperfine tensor ($\mathbf{A}_{Cu}$) are nearly the same.

(v) When the temperature decreases, the average *g*-value remains constant but the anisotropy of the **g** tensor increases. The rhombic anisotropy of the *g*-factor may be defined[34] as $\Delta g_{xy} = (g_2 - g_1)/[{}^1/_2\,(g_1 + g_2) - 2.0023]$. For Cu:Zn(L-asp), $\Delta g_{xy} = 1.303$ at 300 K and $\Delta g_{xy} = 1.386$ at 77 K. In a similar way, we define $\Delta A_{xy} = (A_{Cu}{}^2 - A_{Cu}{}^1)/[{}^1/_2\,(A_{Cu}{}^2 + A_{Cu}{}^1)]$, which increases from $\Delta A_{xy} = 1$ at 300 K to 1.77 at 77 K. As the temperature rises the anisotropies decrease from $\Delta g_{yz} = 0.844$ and $\Delta A_{yz} = 1.878$ at 77 K to $\Delta g_{yz} = 0.596$ and $\Delta A_{yz} = 1.243$ at 300 K.

6. Theoretical Section

In the dynamic E × ϵ formalism,[23,35] the effective vibronic Hamiltonian for a six-coordinated Cu(II) complex is expressed in the normal coordinates Q_θ and Q_ϵ, as[11,17,18]

$$H = H_o + H_{JT} + H_{ST} \tag{4}$$

where

$$H_o = [{}^1/_2 h\nu(P_\theta{}^2 + P_\epsilon{}^2 + Q_\theta{}^2 + Q_\epsilon{}^2) + K_3Q_\epsilon(Q_\theta{}^2 - 3Q_\epsilon{}^2)]\mathbf{U} \tag{4a}$$

$$H_{JT} = A_1(Q_\theta\sigma_z - Q_\epsilon\sigma_x) + A_2[(Q_\theta{}^2 - Q_\epsilon{}^2)\sigma_z + 2Q_\theta Q_\epsilon\sigma_x] \tag{4b}$$

$$H_{ST} = S_\theta\sigma_z - S_\epsilon\sigma_x \tag{4c}$$

with

$$\sigma_x = \begin{bmatrix} 0 & 1 \\ 1 & 0 \end{bmatrix}, \quad \sigma_z = \begin{bmatrix} 1 & 0 \\ 0 & -1 \end{bmatrix}, \quad \mathbf{U} = \begin{bmatrix} 1 & 0 \\ 0 & 1 \end{bmatrix}$$

H_o of eq 4a includes the ionic kinetic energy operator and the potential energy for the nuclear motions, which considers harmonic and anharmonic (K_3) contributions. In the absence of the Jahn-Teller effect, $h\nu$ is the energy of the ϵ_g vibration. H_{JT} of eq 4b contains the first (A_1) and second-order (A_2) Jahn-Teller coupling. H_{ST} of eq 4c acts as a perturbation and considers the lattice strain contribution. It is written in terms of the tetragonal (S_θ) and the orthorhombic (S_ϵ) components and accounts for random and nonrandom strains in the lattice.

TABLE 3: Eigenvalues and Eigenvectors of the g, A_{Cu}, and A_N Tensors for Cu:Zn(L-asp) in the Crystal Axis System (*a, b, c*) for the Site I (shown in Figure 1)[b]

	300 K		77 K		5 K
g_1	2.0377(5)	(0.387,0.844,0.370)	2.028(1)	(0.385,0.822,0.423)	2.03(1)
g_2	2.1701(5)	(−0.379,0.508,−0.774)	2.144(2)	(−0.354,0.552,−0.755)	2.12(3)
g_3	2.3127(4)	(−0.841,0.161,0.517)	2.351(2)	(−0.852,0.143,0.503)	2.36(3)
A_{Cu}^1	61.5(4)	(0.409,0.845,0.344)	58.0(3)	(0.232,0.886,0.401)	55(1)
A_{Cu}^2	20.5(1)	(−0.419,0.508,−0.753)	3.6(3)	(−0.482,0.463,−0.744)	$\|A_{Cu}^2\| = 4(2)$
A_{Cu}^3	87.8(2)[a]	(−0.811,0.164,0.562)	114.5(4)	(−0.845,0.021,0.534)	117(3)
A_N^1			11(2)[a]	(0.48,0.87,0.10)	
A_N^2			11(2)	(−0.34,0.29,−0.89)	
A_N^3			8(3)	(−0.81,0.39,0.44)	

[a] The eigenvalues of $\mathbf{A}_{Cu}$ and of $\mathbf{A}_N$ are given in units of 10^{-4} cm^{-1}. Numbers in parentheses are uncertainties in the last digit. [b] Data at 300 and 77 K are obtained from the EPR spectra of single-crystal samples at X-band and at 5 K from the powder spectrum at Q-band.

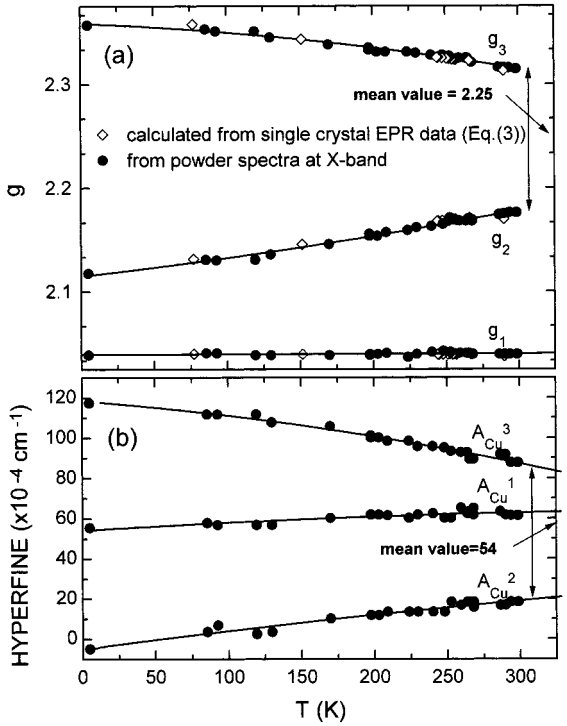

Figure 8. (a) Temperature dependence of the principal values of the **g** tensor. (b) Temperature dependence of the principal values of the $\mathbf{A}_{Cu}$ tensor.

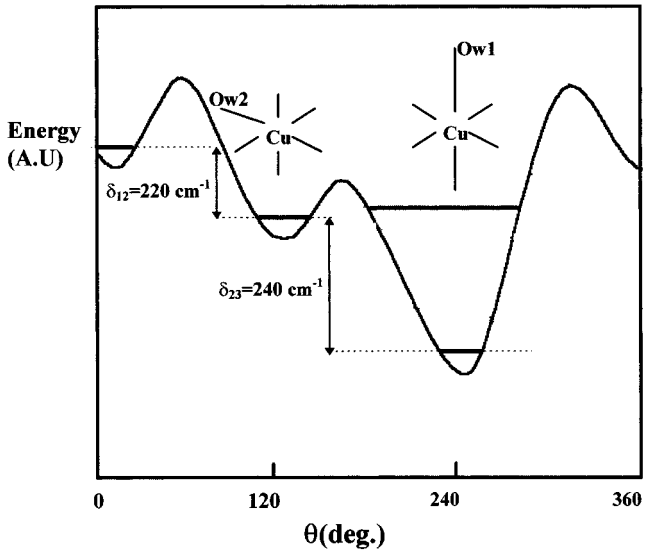

Figure 9. Circular section of the potential surface associated with the three Jahn-Teller wells. The geometric structures of the "isomers" associated with the two lowest vibronic levels are shown.

For cubic structures of identical ligands without random strains, the harmonic approximation ($K_3 = 0$ in eq 4a) with linear Jahn-Teller coupling ($A_2 = 0$ in eq 4b) leads to the "Mexican hat" potential energy surface in the Q_i space.[35−36] There is a minimum stabilization energy at a radial distortion ρ, and therefore an infinite number of equivalent molecular configurations are allowed. When second-order vibronic coupling and the anharmonic term are considered, the potential surface is warped. It displays three equivalent wells with minima at $\varphi = 0$, 120, and 240° corresponding to octahedral geometries tetragonally elongated along the *x*, *y*, and *z* axes. The saddle-points correspond to compressed tetragonal geometries which occur at $\varphi = 60$, 180, and 300°. The height of the barriers separating adjacent wells is 2β and is related to the second-order Jahn-Teller coupling (A_2).[35] This result has been used to explain electronic structures of many copper complexes, characterized by axially symmetric **g** and $\mathbf{A}_{Cu}$ hyperfine tensors at low temperature, which change to isotropic at higher temperature. Tunneling transitions between the minima and variations of the thermal population of the vibronic states are invoked to interpret the changes.[18,20,23,37]

In low-symmetry structures, due either to nonequivalent ligands or distortions of the crystal environment, a "strain" is added through the H_{ST} term (eq 4c). The three wells are no longer equivalent in energy.[18] A negative value of S_θ implies a compression along the principal direction of the strain (i.e., *x*). A positive value of S_ϵ implies a compression along *y* and an elongation along *z*. The differences in strain components produce the energy landscape shown in Figure 9 and define the preferred direction of the Jahn-Teller distortion.

The RH model,[17,18] based on eq 4, is suitable for the description of structural and spectroscopic properties of complexes with six chemically equivalent ligand atoms, assuming that the strain term does not destroy the symmetry of the cubic part of the Hamiltonian. Within this approximation, a low-symmetry complex can be analyzed considering only the first (A_1) and second-order (A_2) Jahn-Teller coupling and one harmonic vibrational force constant, instead of the several constants strictly required by the problem. This model has been applied successfully to "pseudo-Jahn-Teller" complexes, such as the three centers *trans*-$Cu(H_2O)_2Cl_4^{2-}$, *trans*-$Cu(NH_3)_2Cl_4^{2-}$, and *trans*-$Cu(H_2O)(NH_3)Cl_4^{2-}$, in Cu(II)-doped NH_4Cl.[21] The energy levels and wave functions are obtained by diagonalizing the matrix of the Hamiltonian of eq 4 in a set of vibronic basis functions formed by the $E_g(d_{x^2-y^2}, d_{z^2})$ metal orbital wave functions and the *N* harmonic oscillator wave functions of the ϵ_g vibration. The differences between vibronic levels are larger than the Zeeman splitting, and the magnetic field produces no mixing of the states. Each vibronic level has its own set of

g-values that are calculated from the electronic part of its wave function as is described in ref 18. If vibronic relaxation between these levels is faster than the EPR time of measurement, the observed *g*-values correspond to a Boltzmann average over them. Thus, the temperature dependence of the **g** tensor is accounted in terms of the population of the vibronic levels by the intrawell and interwell dynamics.[18] To a good approximation, the effect of the strain in the RH model is to break the energy degeneracy of the wells and thus to localize the lowest vibronic levels in the lowest well (see Figure 9). If the hopping rate between the wells is slower than the EPR time scale, the *g*-values observed at low temperature are associated to the individual levels localized in the lowest well for a specific molecular configuration and, thus, they provide the molecular *g*-values. Due to vibronic mixing of the nondegenerate electronic state with close excited states, the ground vibronic state has a set of *g*-values characteristic of an orthorhombic tensor. The electronic part of the lowest energy state at this static geometry is an appropriate linear combination of the $(d_{x^2-y^2})$ and (d_{z^2}) orbitals so that the wave function has the largest lobe along *x*, the intermediate one along *y*, and the shortest along *z*, in accordance with the experimental data at low temperature. When the temperature is raised, changes in the *g*-values are interpreted as due to the changes in the Boltzmann populations of the vibronic levels of the different wells. As higher vibronic levels are delocalized, they allow rapid exchange among the wells.

Strictly, in a low-symmetry problem, the environment removes the degeneracy of the electronic states. A tetragonal elongation on the octahedral symmetry of the Cu(II) site produces the splitting of the ^2E_g state into $^2B_{1g}$ $(d_{x^2-y^2})$ and $^2A_{1g}$ (d_{z^2}) states, with the energy of the former lower than the latter. The three T_{2g} states split into $^2B_{2g}$ (d_{xy}) and ^2E_g (d_{xz}, d_{yz}) states. Similarly, angular distortions on the ligand bonds in the equatorial plane or replacement of some coordinated atoms by others contribute to split the degeneracy of the ^2E_g states. Therefore, a set of electronic energy levels E_0^i are defined instead of one degenerate energy level as in high symmetry complexes. If any of these states is sufficiently close to the ground state, a strong "pseudo-Jahn-Teller" effect is not quenched and contributes to stabilize the complex with a minimum energy $E_{JT} < \Delta/2$ (where Δ is the energy splitting between the two lowest states). Therefore, the strong vibronic coupling produces a structural angular distortion of the wells in the Q_i space (pseudo-Jahn-Teller effect). For ions in sites with no symmetry, the energy of the distorted complex is different for each well due to the difference in the environment.[26] This fact is reflected in the angular part of the potential surface, such as that shown in Figure 9, similar to those communicated by Riley et al.[18] for S_θ and S_ϵ values between -550 and -800 cm^{-1}, and 110 and 200 cm^{-1}, respectively. Therefore, the RH model can be used as a good approximation to analyze a low-symmetry problem.

In comparison, the simple SG model[16] for a low-symmetry complex is based in a similar potential surface and retains the features of a strong Jahn-Teller system. However, the Jahn-Teller stabilization energy is in this case larger than the energy of the vibrational modes. Therefore, the temperature dependence is interpreted as the dynamic equilibrium between different Jahn-Teller distorted "isomer" configurations associated with each well. These isomers have identical geometry and *g*-values but different orientations of the molecular axes. The temperature behavior depends on the Boltzmann population of these configurations. In fact, this model approaches the RH model when the lowest vibronic wave functions are strongly localized in separate minima in both senses, electronic and geometric. In our description of the temperature dependence of the magnetic parameters detected in our EPR experiments we use later the SG model.

The principal ideas to be used in the analysis of our experimental results within the framework of the SG model, as an approximation to the RH model, are as follows.

(i) There is a vibronic mixing of a nondegenerate electronic ground state with near excited states. The copper ion orbital part of the ground-state wave function is mainly a mixture of $d_{x^2-y^2}$ and d_{z^2} orbitals.

(ii) Each vibronic state has a set of *g*-values characteristic of an orthorhombic tensor.

(iii) Due to the lattice strains S_θ and S_ϵ, the potential energy surface has wells with different energy minima.

(iv) If the levels are localized at different wells, the temperature dependence of the *g*-values results as the Boltzmann average over two distorted "isomer" configurations.

(v) The molecular geometry at different wells shows an interchange of the bond lengths, characteristic of the "isomer" configuration.

7. Discussion

7.1. Symmetry and Lattice Distortions at the Cu Site in Cu:Zn(L-asp). The symmetry at the Zn sites when they are occupied by Cu impurities is the result of the demands of the lattice and the tendency of the complex to undergo Jahn-Teller distortions. To get information about the distortions, we compare the EPR results reported here for Cu:Zn(L-asp) with those obtained for Cu in Cu(L-asp).[5] The single EPR line observed by Calvo et al. for Cu(L-asp) at 300 K is the result of the collapse of the resonances of the magnetically nonequivalent sites in the unit cell due to the exchange interactions. This collapse blurs information about local properties of the copper ions, such as symmetry related sites and hyperfine couplings with the copper nuclei and with the nitrogen ligand. The reported **g** tensor is an average of the molecular **g** tensor for copper ions at the two magnetically nonequivalent sites. The molecular value of $g_\parallel = 2.312$, calculated for Cu(II) in Cu(L-asp) assuming axial molecular symmetry, coincides with the value of g_3 for Cu(II) in Cu:Zn(L-asp). Their principal directions, perpendicular to the mean-square plane defined by the O1, O3′, N, and Ow2 ligands (see Figure 2), agree within experimental uncertainties. For Cu(L-asp), it was obtained $g_\perp = 2.089$ which should be compared with the values of g_1 and g_2 in Table 3. Thus, it seems that the hypothesis of axial symmetry in this plane for Cu(L-asp) was not a good assumption. As shown in Figure 7, the principal directions corresponding to g_1 and g_2 for Cu(II) in Cu:Zn(L-asp) form angles of 4.8° and 7.7° with the Zn−N and Zn−Ow2, respectively. These angles are similar to those calculated for g_x and g_y (*x*, *y* axes in the equatorial plane) in Cu(II)-doped single crystals of bis(L-histidinato)cadmium dihydrate[38] and L-histidine hydrochloride monohydrate.[39]

The difference between the Zn−Ow1 and Zn−Ow2 bond lengths is smaller than those in the copper complex (∼0.07 compared with ∼0.37). In Zn(L-asp) Ow2, Ow1, and N ligands exhibit almost spherically symmetric thermal ellipsoids with mean radius of the order of 0.15 Å. In the copper complex, the thermal ellipsoids are more anisotropic with distortions along the Cu−Ow1 and Cu−Ow2 bond directions. This would indicate some dynamic disorder of Ow1 and Ow2 along these bond directions when the Cu ion substitutes the Zn ion in the diluted sample.[26−40] The long, intermediate, and short metal−ligand bonds occur in the same directions in Cu(L-asp) as in the host

complex. The similarity in the bond angles of Zn(L-asp) and Cu(L-asp) shown in Table 2 (except for the displacement of the N ion produced by the aspartate tridentate coordination) indicates that distortions involve the metal−ligand directions.

We conclude that Cu(II) distorts the host lattice structure to adopt the octahedral geometry of the pure complex in the direction of a water oxygen. The long, medium, and short bonds occur in similar directions in Cu(L-asp) and Zn(L-asp). The orthorhombic **g** and $\mathbf{A}_{Cu}$ tensors in Zn(L-asp) reflect the presence of nonequivalent ligands and the important angular distortion (angle N−metal−O1 ≈ 78°). Since the largest value g_3 is along the perpendicular to the equatorial plane, the tetragonal distortion dominates the site symmetry and, as $g_1 \neq g_2$ with the principal direction along the metal−ligand bonds, we may assume an approximate D_2 symmetry to simplify the problem in the discussion below.[41]

7.2. Molecular *g*-Values and Hyperfine Coupling. The copper ground-state orbital wave function is a linear combination of the $d_{x^2-y^2}$ and d_{z^2}.[39,42] The $d_{x^2-y^2}$ orbital is associated to the Cu(II) ion in a elongated octahedral configuration of negatively charged ligands[43] and the d_{z^2} mixing in the ground state produces the anisotropy of the **g** and $\mathbf{A}_{Cu}$ tensors in the equatorial plane with the principal directions close to the metal−ligand bond.[34,44] The copper ground-state orbital wave function can be written as

$$\Psi = a d_{x^2-y^2} - b d_{z^2} \tag{5}$$

where a and b are the mixing coefficients that satisfy the normalization condition $a^2 + b^2 = 1$.

In terms of these coefficients, the principal values of the **g** and $\mathbf{A}_{Cu}$ tensors can be expressed as[22,45,46]

$$g_x = g_e - 2\alpha^2\lambda(a - b\sqrt{3})^2/E_{yz} \tag{6a}$$

$$g_y = g_e - 2\alpha^2\lambda(a + b\sqrt{3})^2/E_{xz}$$

$$g_z = g_e - 8\alpha^2\lambda a^2/E_{xy}$$

$$A_{Cu}{}^x = P_0[-\alpha^2 K + 2/7\alpha^2(a^2 - b^2) - 4/7\sqrt{3}\alpha^2 ab + \Delta g_x - (3a - b\sqrt{3})\Delta g_y/14(a + b\sqrt{3}) - b\sqrt{3}\Delta g_z/14a] \tag{6b}$$

$$A_{Cu}{}^y = P_0[-\alpha^2 K + 2/7\alpha^2(a^2 - b^2) - 4/7\sqrt{3}\alpha^2 ab + \Delta g_y - (3a + b\sqrt{3})\Delta g_x/14(a - b\sqrt{3}) + b\sqrt{3}\Delta g_z/14a]$$

$$A_{Cu}{}^z = P_0[-\alpha^2 K + 4/7\alpha^2(a^2 - b^2) + (3a - b\sqrt{3})\Delta g_y/ 14(a + b\sqrt{3}) + (3a + b\sqrt{3})\Delta g_x/14(a - b\sqrt{3}) + \Delta g_z]$$

where $g_e = 2.0023$ is the free electron value, $\lambda = -828$ cm^{-1} is the spin−orbit coupling constant for the free Cu(II) ion, E_{ij} is the energy of the excited state in which the unpaired electron occupies the d_{ij} orbital, $\Delta g_{x,y,z}$ are the g shifts from the free-electron value, $g_N(^{63}Cu) = 1.4804$ is the nuclear g-factor of ^{63}Cu, and μ_N is the nuclear magneton. For the free copper ion the parameter $P_0 = g_e g_N \mu\mu_N \langle r^{-1}\rangle = 0.036$ cm^{-1} and the Fermi contact parameter $K = 0.43$.[45] We assume that at 5 K the copper ions adopt the lowest energy configuration and the molecular g-values and copper hyperfine tensors are those obtained from the powder spectrum at that temperature (see Table 3). For the electronic components of the lowest vibronic wave functions, the expectation values of the squares of the parameters are $a^2 = 0.94$ and $b^2 = 0.048$ from eq 6. Therefore, the unpaired electron essentially occupies a $d_{x^2-y^2}$ orbital, with a slight admixture of d_{z^2}.

7.3. Vibronic Effects. The fact that the traces of the **g** and hyperfine tensors do not change with temperature (see Table 3) indicates that no structural transitions occur in the studied range. Thus, we are going to analyze the temperature dependence of the g and copper hyperfine values in terms of the coupling between unpaired electron and vibronic states. As the temperature is raised, the observed values of g_2 and g_3 ($A_{Cu}{}^2$ and $A_{Cu}{}^3$) approach mean values $g = 2.25$ and $A_{Cu} = 54 \times 10^{-4}$ cm^{-1}, equal to those found from the powder data at 5 K. This fact is indicative of a dynamic averaging process[47] as assumed in the SG[16] and RH [17,18] models where the nonequivalence of the wells[8] is due to the presence of nonequivalent ligands (see Figure 9). This potential surface reflects the strain effects of the lattice and the preferred direction of the Jahn-Teller distortion. The tetragonal strain (S_θ) is related to the energy difference between the $d_{x^2-y^2}$ and d_{z^2} orbitals in Cu(L-asp) with the appropriate metal−ligand bonds for a regular octahedral geometry ($\delta E/2 = S_\theta$).[21] Therefore, we find the sign of S_θ from the difference in the σ bonds between the axial and in-plane ligands through[8]

$$\mathbf{S}_\theta = V_2 \mathbf{e}_\theta = V_2[e_{zz} - {}^1/_2(e_{xx} + e_{yy})] \tag{7}$$

$$\mathbf{S}_\epsilon = V_2 \mathbf{e}_\epsilon = \sqrt{3}/2 V_2(e_{xx} - e_{yy})$$

where V_2 is a strain coupling coefficient and e_{xx}, e_{yy}, and e_{zz} are the diagonal components of the strain tensor. As Cu(L-asp) has different ligands, we get information on S_θ comparing the σ-bonding strength from the spectrochemical sequence $H_2O <$ $NH_3 <$ ... $< OC^-$. The z and y axes involve similar σ bonds, weaker than that along the x axis. Therefore, we conclude that the tetragonal strain (S_θ) is negative and reflects a compression acting along the shortest Cu−N direction. Thus, the energy of the well 1 is δ_{13} above the lower well. The orthorhombic lattice strain component (S_ϵ) is positive and defines the energy difference δ_{23} between the two lower nonequivalent wells. Therefore, distortions of the Cu−water oxygen bond lengths require less energy. These correspond to distorted configurations with the long bond occurring along the Cu−Ow2 (well 2) or the Cu−Ow1 (well 3) directions. Figure 9 illustrates the isomer configurations associated with the two lowest wells 2 and 3 in the SG model. The "zero-temperature" values of the tensors **g** and $\mathbf{A}_{Cu}$ measured at 5 K (see Table 3) correspond to those of the molecule localized in the ground vibronic level of well 3. As described by the SG model, at higher temperature, the molecule may distort along the Cu−Ow2 direction jumping to the well 2. We also assume that the structural isomers have similar magnetic parameters but with the directions of the distortion interchanged. Thus, the calculated eigenvalues $g_i(T)$ and $A_{Cu}{}^i(T)$ are the Boltzmann averages:[47]

$$g_1 = n_1 g_{30} + n_2 g_{10} + n_3 g_{10} \tag{8a}$$

$$g_2 = n_1 g_{20} + n_2 g_{30} + n_3 g_{20}$$

$$g_3 = n_1 g_{10} + n_2 g_{20} + n_3 g_{30}$$

$$A_{Cu}{}^1 = n_1 A_{Cu}{}^{30} + n_2 A_{Cu}{}^{10} + n_3 A_{Cu}{}^{10} \tag{8b}$$

$$A_{Cu}{}^2 = n_1 A_{Cu}{}^{20} + n_2 A_{Cu}{}^{30} + n_3 A_{Cu}{}^{20}$$

$$A_{Cu}{}^3 = n_1 A_{Cu}{}^{10} + n_2 A_{Cu}{}^{20} + n_3 A_{Cu}{}^{30}$$

where $n_1 + n_2 + n_3 = 1$.

The ratio K_{ij} between each pair i,j of fractional populations is related to the energy difference between the isomer configura-

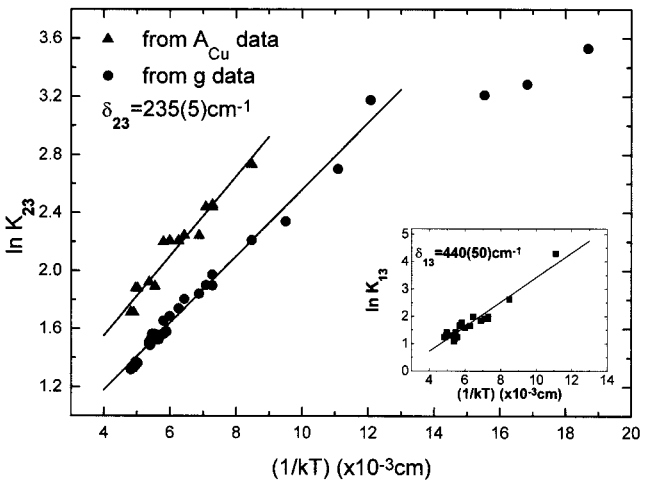

Figure 10. Plot of ln K_{23} vs $(kT)^{-1}$ where $K_{23} = n_2/n_3$ is the ratio of the populations of the wells 2 and 3, as derived from the g and A_{Cu} values, shown in Figure 8. In the inset, we plot ln K_{13} vs $(kT)^{-1}$ with $K_{13} = n_1/n_3$ being the ratio of the populations of the wells 1 and 3, calculated from the temperature dependence of the A_{Cu} values.

tions by[16]

$$K_{ij} = n_i/n_j = \exp(\delta_{ij}/kT) \tag{9}$$

As $g_1(T)$ is temperature independent, the higher well is not significantly populated in the studied temperature range and is not considered in the analysis. The ratio K_{23} is obtained using eq 8a and the data of $g_2(T)$ and $g_3(T)$ (see Figure 8), and also using eq 8b and the data of $A_{Cu}^2(T)$ and $A_{Cu}^3(T)$ (Figure 8). We calculate an energy difference $\delta_{23} = 235(5)$ cm^{-1} (from the g values) and 250(10) cm^{-1} (from the A_{Cu} values) between the wells 2 and 3 using eq 9 and the linear plot of ln K vs $(kT)^{-1}$ (see Figure 10). Differences of the order of 5% between the values of K_{23}, calculated from the g and A_{Cu} data, are attributed to the uncertainties of A_{Cu}^{20} and A_{Cu}^{30} obtained from the powder spectrum at 5 K. This result suggests the validity of the SG model in the temperature range 100−300 K. An energy difference $\delta_{13} \approx 440(50)$ cm^{-1} may be calculated from the weak temperature dependence of A_{Cu}^1. However, the fact that the tensors **g** and $\mathbf{A}_{Cu}$ are orthorhombic and temperature dependent between 5 and 100 K, with δ_{23} temperature dependent, requires further explanation. It suggests that below 100 K well 2 is not populated. This may be attributed to the following.

(a) A possible resolution of the EPR spectra of the two wells due to a jumping rate between them slower than the EPR time scale.[47] Therefore, the spectra below 100 K should show additional resonance lines of low intensity related to the complex at the well 2.

(b) The complex is strongly localized in the well 3 due to the lattice strains. This behavior is characteristic of a strong Jahn-Teller effect. As temperature increases transitions to excited vibronic levels located in the same well should account for the observed temperature dependence. In this case, the RH model is compatible with the experimental results in the (5−300 K) range of temperature.

(c) The shape of the potential surface may change with temperature as a result of a cooperative effect of the neighboring Zn ions. This would happen because the bridging nature of the aspartate cannot take up the strain caused by the Cu(II) ion. Taking into account the structure of the aspartate, the only possible deformation that it can suffer seems to be through the C−O bonds of the carboxylate group. The Jahn-Teller elongation in the Cu−Ow1 can produce a shortening of the C4−O4 bond with the concomitant elongation of the C4−O3 bond, in the range of a few angstroms admitted by the simple double C−O bonds, which would affect the neighbor Zn site.

As no additional EPR lines were detected at 5 K, our results suggest that (a) may not be a plausible explanation. Due to the lack of experimental data involving the Zn sites, cooperative effects cannot be analyzed in this paper in order to decide between possibilities (b) and (c).

8. Conclusions

The EPR spectra of Cu:Zn(L-asp) suggest that the complex has a tetragonally elongated octahedral local geometry with an orthorhombic distortion. Comparisons between the crystal structures of Zn(L-asp) and Cu(L-asp) indicate that when Cu(II) ions substitute the Zn ions in diluted samples, they adopt a geometry similar to that of the pure complex. The orthorhombic **g** and $\mathbf{A}_{Cu}$ tensors reflect the presence of nonequivalent ligands and an important angular distortion associated with the metal−N bond. From the molecular g-values at 5 K, we conclude that the hypothesis of axial symmetry assumed by Calvo et al.[5] for Cu(L-asp) may not be a good one. Our result provides information about the molecular structure of this complex. The ground state is $d_{x^2-y^2}$ with a small admixture of d_{z^2} which takes into account the anisotropy of the **g** and $\mathbf{A}_{Cu}$ tensors in the equatorial plane.

The spectra between 5 and 300 K show an important temperature dependence of the eigenvalues of **g** and $\mathbf{A}_{Cu}$. However, the eigenvectors do not change with temperature. The eigenvector corresponding to the lowest g-value is along the Zn−N bond, while the other two, oriented along the Zn−Ow directions, are involved in the dynamic Jahn-Teller distortions. The highly orthorhombic **g** and $\mathbf{A}_{Cu}$ tensors are due to the weighted average of the two structural isomers in thermal equilibrium above 100 K, with the Jahn-Teller elongation along each of the (Cu−Ow) directions. The aspartate ion acts as a rigid structure and restricts the nuclear movement along the third direction. The dynamic behavior in Cu(II)-doped Zn(L-asp) can be explained considering a three-well adiabatic potential surface. In this asymmetric environment, the complex is influenced by lattice strains. These are described in terms of the tetragonal and orthorhombic lattice strain components S_θ and S_ϵ. These strains produce differences in the energy between the wells. Above 100 K, the dynamic behavior may be explained with the SG model, assuming an energy splitting $\delta_{23} = 235(5)$ cm^{-1} between the lowest wells 2 and 3, associated with the (Cu−Ow) directions. The third well, with an energy difference $\delta_{13} \approx 440(50)$ cm^{-1}, is not populated in the range 100−300 K. Therefore, the Jahn-Teller distortions may involve the water directions. The "zero-temperature" molecular geometry reflects the orthorhombic symmetry characteristic of a "pseudo-Jahn-Teller" complex. In Cu(L-asp), this behavior may be similar and two different configurations could be present even at 300 K, a fact which was not detected in ref 5. Further experimental data between 5 and 100 K would confirm that. At low temperature, the complex is strongly localized in the deepest well reflecting a strong static Jahn-Teller effect, with possible transitions to excited vibronic levels, as assumed in the RH model.

Acknowledgment. We thank Profs. E. E. Castellano and J. Zuckerman-Schpector for providing us new X-ray crystallographic data for Zn(L-asp). Work supported by the Universidad Nacional del Litoral (CAID 96-00-010-055) and CONICET (PMT-PICT 0055).

References and Notes

(1) Lippard, S. J.; Berg, J. M. *Principles of Bioinorganic Chemistry*; University Science Books: Mill Valley, 1994; Chapters 1 and 3.

(2) Doyne, T.; Pepinsky, R.; Watanabe, T. *Acta Crystallogr*. **1957**, *10*, 438.

(3) Kryger, L.; Rasmussen, S. E. *Acta Chem. Scand*. **1973**, *27*, 2674.

(4) Antolini, L.; Menabue, L.; Pellacani, G. C.; Marcotrigiano, G. *J. Chem. Soc., Dalton Trans*. **1982**, 2541.

(5) Calvo, R.; Steren, C. A.; Piro, O. E.; Rojo, T.; Zuñiga, F. J.; Castellano, E. E. *Inorg. Chem*. **1993**, *32*, 6016.

(6) Castellano, E. E.; Zuckerman-Schpector, J. Unpublished results. We are grateful to these authors for allowing us to use their results.

(7) Pake, G. *Paramagnetic Resonance*, 1st ed.; W. A. Benjamin: New York, 1962; Chapter 7.

(8) Ham, F. S. *Phys. Rev*. **1968**, *166*, 307.

(9) O'Brien, M. C. M. *Proc. R. Soc. A* **1964**, *281*, 323.

(10) O'Brien, M. C. M. *Phys. Rev.* **1969**, *187*, 407.

(11) Abragam, A.; Bleaney, B. *Electron Paramagnetic Resonance of Transition Ions*; Clarendon Press: Oxford, 1970; Chapter 21.

(12) Öpik, U.; Pryce, M. H. L. *Proc. R. Soc. A* **1957**, *238*, 425.

(13) Moffitt, W.; Lehr, A. D. *Phys. Rev.* **1957**, *106*, 1195.

(14) Reinen, D.; Friebel, C. *Struct. Bonding* **1979**, *37*, 1.

(15) Moffitt, W.; Thorson, W. *Phys. Rev.* **1957**, *108*, 1251.

(16) Silver, B. L.; Getz, D. *J. Chem. Phys*. **1974**, *61*, 638.

(17) Riley, M. J.; Hitchman, M. A.; Reinen, D. *Chem. Phys.* **1986**, *102*, 11.

(18) Riley, M. J.; Hitchman, M. A.; Wan Mohammed, A. *J. Chem. Phys*. **1987**, *87*, 3766.

(19) Wang, D. M.; Kovacik, I.; Reijerse, E. J.; de Boer, E. *J. Chem. Phys*. **1992**, *97*, 3897.

(20) Headlam, H.; Hitchman, M. A.; Stratemeier, H.; Smits, J. M. M.; Beurskens, P. T.; de Boer, E.; Janssen, G.; Gatehouse, B. M.; Deacon, G. B.; Ward, G. N.; Riley, M.; Wang, D. *Inorg. Chem.* **1995**, *34*, 5516.

(21) Riley, M. J.; Hitchman, M. A.; Reinen, D.; Steffen, G. *Inorg. Chem.* **1988**, *27*, 1924.

(22) Hoffmann, S. K.; Goslar, J.; Szczepaniak, L. S. *Phys. Status Solidi B* **1986**, *133*, 321.

(23) Bersuker, I. B. *Electronic Structure and Properties of Transition Metal Compounds*; Wiley: New York, 1996; Chapters 7 and 9. Bersuker, I. B. *The Jahn-Teller Effect and Vibronic Interactions in Modern Chemistry*; Plenum: New York, 1984; Chapters 2−4.

(24) Battaglia, L. P.; Bonamartini Corradi, A.; Antolini, L.; Marcotrigiano, G.; Menabue, L.; Pellacani, G. C. *J. Am. Chem. Soc*. **1982**, *104*, 2407.

(25) Battaglia, L. P.; Bonamartini Corradi, A.; Marcotrigiano, G.; Menabue, L.; Pellacani, G. C. *J. Am. Chem. Soc*. **1980**, *102*, 2663.

(26) Stebler, M.; Bürgi, H. *J. Am. Chem. Soc*. **1987**, *109*, 1395.

(27) Weil, J. A. *J. Magn. Reson*. **1975**, *18*, 113.

(28) Calvo, R.; Oseroff, S. B.; Abache, H. C. *J. Chem. Phys*. **1980**, *72*, 760.

(29) Isaacson, R. A.; Lendzian, F.; Abresch, E. C.; Lubitz, W.; Feher, G. *Biophys. J.* **1995**, *69*, 311.

(30) Nilges, M. J. Ph.D. Thesis, University of Illinois, Urbana, Illinois, 1979.

(31) Belford, R. L.; Nilges, J. Computer Simulation of Powder Spectra. EPR Symposium, 21st Rocky Mountain Conference, Denver, Colorado, 1979.

(32) Maurice, A. M. Ph.D. Thesis, University of Illinois, Urbana, Illinois, 1980.

(33) Bleaney, B.; Bowers, K. D.; Ingram, D. J. E. *Proc. R. Soc*. **1955**, *A228*, 147.

(34) Hitchman, M. A.; Olson, C. D.; Belford, R. L. *J. Chem Phys*. **1969**, *50*, 1195.

(35) Ham, F. S. In *Electron Paramagnetic Resonance;* Geschwind, S., Ed.; Plenum: New York, 1972; Chapter 1.

(36) Bersuker, I. B. *Coord. Chem. Rev.* **1975**, *14*, 357.

(37) Astley, T.; Headlam, H.; Hitchman, M.; Keene, F. R.; Pilbrow, J.; Stratemeier, H.; Tiekink, E.; Zhong, Y. *J. Chem. Soc., Dalton Trans*. **1995**, 3809.

(38) Colaneri, M. J.; Peisach, J. *J. Am. Chem. Soc*. **1995**, *117*, 6308.

(39) Hirasawa, R.; Kon, H. *J. Chem. Phys*. **1972**, *56*, 4467.

(40) Ammeter, J. H.; Bürgi, H. B.; Gamp, E.; Meyer-Sandrin, V.; Jensen, W. P. *Inorg. Chem*. **1979**, *18*, 733.

(41) Hathaway, B. J.; Billing, D. E.; Nicholis, P.; Procter, I. M. *J. Chem. Soc. A* **1969**, 319.

(42) Hitchman, M. A. *J. Chem. Soc. A* **1970**, 4.

(43) Steren, C. A.; Calvo, R.; Piro, O. E.; Rivero, B. E *Inorg. Chem*. **1989**, *28*, 1933.

(44) Bacci, M.; Cannistraro, S. *Chem. Phys. Lett.* **1986**, 109.

(45) Hitchman, M. A. *Inorg. Chem*. **1985**, *24*, 4762.

(46) Deeth, R. J.; Hitchman, M. A.; Lehmann, G.; Sachs, H. *Inorg. Chem*. **1984**, *23*, 1310.

(47) Hoffmann, S. K.; Goslar, J.; Hilczer, W.; Augustyniak, M. A.; Marciniak, M. *J. Phys. Chem. A* **1998**, *102*, 1697.